

# Large-area narrowband Fabry–Pérot interferometers for long-wavelength infrared spectral sensing

Gurpreet Singh Gill<sup>a,\*</sup>, Michal Zawierca<sup>a</sup>, Dharendra Kumar Tripathi,<sup>a</sup> Adrian Keating,<sup>b</sup> Gino Putrino,<sup>a</sup> Konkaduwa Kamala Mesthrige Buddhika Dilusha Silva,<sup>a</sup> Lorenzo Faraone,<sup>a,c</sup> and Mariusz Martyniuk<sup>a,c</sup>

<sup>a</sup>The University of Western Australia, Department of Electrical, Electronic and Computer Engineering, Perth, Western Australia, Australia

<sup>b</sup>The University of Western Australia, Department of Mechanical Engineering, Perth, Western Australia, Australia

<sup>c</sup>The University of Western Australia, ARC Centre of Excellence on Transformative Meta-Optical Systems (TMOS), Perth, Western Australia, Australia

**Abstract.** This paper presents a proof-of-concept for microelectromechanical system (MEMS)-based fixed cavity Fabry–Pérot interferometers (FPIs) operating in the long-wavelength infrared (LWIR, 8 to 12  $\mu\text{m}$ ) region. This work reports for the first time on the use of low-index BaF<sub>2</sub> thin films in combination with Ge high-index thin films for such applications. Extremely flat and stress-free  $\sim 3\text{-}\mu\text{m}$ -thick free-standing distributed Bragg reflectors (DBRs) are also presented in this article, which were realized using thick lift-off of a trilayer structure fabricated using Ge and BaF<sub>2</sub> optical layers. A peak-to-peak flatness was achieved for free-standing surface micromachined structures within the range of 10 to 20 nm across large spatial dimensions of several hundred micrometers. Finally, the optical characteristics of narrowband LWIR fixed cavity FPIs are also presented with a view toward the future realization of tunable wavelength MEMS-based spectrometers for spectral sensing. The measured optical characteristics of released FPIs agree with the modeled optical response after taking into consideration the fabrication-induced imperfections in the free-standing top DBR such as an average tilt of 15 nm and surface roughness of 25 nm. The fabricated FPIs are shown to have a linewidth of  $\sim 110$  nm and a suitable peak transmittance value of  $\sim 50\%$ , which meets the requirements for their utilization in tunable MEMS-based LWIR spectroscopic sensing and imaging applications requiring spectral discrimination with narrow linewidth. © The Authors. Published by SPIE under a Creative Commons Attribution 4.0 International License. Distribution or reproduction of this work in whole or in part requires full attribution of the original publication, including its DOI. [DOI: [10.1117/1.JOM.2.2.023502](https://doi.org/10.1117/1.JOM.2.2.023502)]

**Keywords:** microelectromechanical systems; microspectrometers; Fabry–Pérot interferometer; optical thin films; peak transmission; linewidth; infrared filters; spectral sensing and imaging; distributed Bragg reflectors.

Paper 22002G received Jan. 28, 2022; accepted for publication Apr. 22, 2022; published online May 19, 2022.

## 1 Introduction

Fabry–Pérot interferometer (FPI) technologies are commonly used to fabricate microelectromechanical systems (MEMS) based tunable infrared filters.<sup>1–8</sup> In an FPI, two highly reflective mirrors are separated by an air-gap optical cavity that defines the spectral passband position.<sup>9</sup> The length of the air-cavity between the two mirrors is half of the targeted center wavelength. In high-performing MEMS-based FPIs, these distributed Bragg reflector (DBR) mirrors are fabricated by depositing an alternating sequence of low-absorbing quarter-wavelength thick dielectric layers of high- and low-refractive index materials, instead of lossy metal mirrors.<sup>9</sup> High contrast in the refractive indices is the key to producing highly reflective DBRs and to extend the free spectral range (FSR) of the FPI which, in turn, leads to a narrow full width

\*Address all correspondence to Gurpreet Singh Gill, [gurpreet.gill@uwa.edu.au](mailto:gurpreet.gill@uwa.edu.au)

at half maximum (FWHM) of the optical passband and improved out-of-band rejection. The out-of-band rejection is a critical parameter of an FPI, which is expressed as the ratio of the transmission maximum to transmission minimum within the wavelength band of interest. Furthermore, highly reflective DBRs also ensure a higher optical cavity finesse, which is an important FPI figure of merit given by the ratio of FSR and FWHM. The finesse of a MEMS-based FPI will be compromised by any tilt, curvature/distortion, and/or thin-film roughness of the DBRs.<sup>10</sup>

There are numerous published reports on MEMS-based narrowband FPIs in the short-wavelength infrared and midwavelength infrared regions.<sup>6,8,11–17</sup> However, very limited reports are available on MEMS-based narrowband FPIs in the long-wavelength infrared (LWIR) region due to challenges involved in the fabrication processes and the lack of suitable optomechanical materials in the LWIR band. Some of the published studies on LWIR FPIs include surface micromachined narrowband filters using Si-Air-Si based DBRs by VTT,<sup>18,19</sup> which gave an FWHM of 140 nm. Similarly, The University of Western Australia has utilized Ge and ZnS thin films and achieved an FWHM of 500 to 1000 nm, which are suitable for multispectral imaging.<sup>20–23</sup> On the other hand, bulk micromachined narrowband LWIR FPIs have also been fabricated by a group of researchers from InfraTec, and have achieved an FWHM of 105 to 250 nm in the LWIR region.<sup>24–29</sup> Another research group from Teledyne has reported an FWHM of 90 to 120 nm in the LWIR region.<sup>30,31</sup> Thus, in general, bulk micromachined FPIs have been able to provide narrower FWHM in comparison to surface micromachined FPIs. However, the fabrication process of bulk micromachined FPIs is far more complex, since it uses two silicon wafers and is based on a higher cost fabrication technology in comparison to surface micromachined FPIs. This includes the requirement for Au-Au thermocompression and SU-8 bonding, a silicon on insulator device layer transfer process, and the removal of the Si substrate/handling wafer.<sup>24,28,30,31</sup>

Thus far, Si-based technologies using Si as the high-index material in combination with other low-index Si-based materials such as  $\text{SiO}_x$ ,  $\text{SiN}_x$ , and  $\text{SiO}_x\text{N}_y$  have dominated the development of MEMS-based portable FPIs in the IR region. However, since Si-based low-index materials are not suitable for the LWIR (8 to 12  $\mu\text{m}$ ) region due to high absorption losses, this has severely hindered the development of narrowband LWIR FPIs. Although it is possible to develop the narrowband LWIR FPIs using air as a low-refractive index medium along with Si,<sup>18,19</sup> based on the high refractive index contrast provided by the air in combination with Si, this leads to a highly-complex fabrication process requiring multiple air cavities. Therefore, to develop narrowband FPIs for the LWIR region researchers have avoided the use of Si-based MEMS technologies and have examined the use of Ge and ZnS optical thin films to fabricate surface micromachined MEMS-based FPIs.<sup>20–23</sup> However, these FPIs cannot achieve the narrow line-widths required for spectroscopic sensing due to the poor refractive index contrast between the high- and low-refractive index materials. On the other hand,  $\text{BaF}_2$  is a highly attractive optical material due to its low refractive index<sup>32,33</sup> in the LWIR wavelength range and provides high contrast in refractive index, which can significantly improve the performance of LWIR FPIs. Therefore, this work explores the use of germanium (Ge) as the high-index optical thin film along with barium fluoride ( $\text{BaF}_2$ ) as the low-index optical thin film for the development of MEMS-based FPIs. Since MEMS-based FPIs are fabricated using either surface micromachined or bulk micromachined techniques, it becomes critically important to develop a reliable and reproducible fabrication process for the development of high-performing FPIs in the LWIR band utilizing standard thermally evaporated optical layers. The adhesion requirement for each of these layers and other commonly used MEMS materials throughout many wet and dry etching steps used during the fabrication of complex MEMS-based free-standing structures must be addressed. The optical and mechanical properties of these materials have already been presented in our previous studies.<sup>34,35</sup>

This paper reviews the modeling framework for determining the optical properties of an ideal FPI, followed by a study of the effect of fabrication-induced imperfections. Subsequently, a reliable and reproducible fabrication process is presented for surface micromachined fixed cavity LWIR filters based on a free-standing top DBR utilizing a three-layer structure of Ge/ $\text{BaF}_2$ /Ge optical thin films. The complete removal of the sacrificial layers under the free-standing top DBR membranes was verified by taking a cross-section scanning electron micrograph, where the cross-section was prepared using the focused ion beam (FIB) technique. Finally, this paper

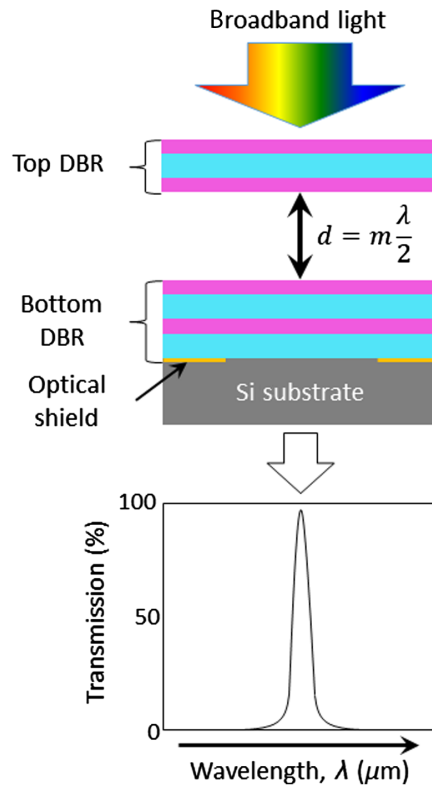
reports on the optical characterization of released fixed air-cavity filters, and compares the measured optical performance with the modeled results and previous studies. The impact of fabrication-induced imperfections on the DBRs is also reported in this article.

## 2 Fundamentals of Fabry–Pérot Interferometers

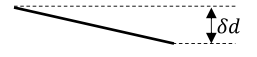
Multiple-beam interferometers form a class of interferometers in which multiple beams are confined in an optical cavity between two mirror plates or DBRs to realize MEMS-based FPIs.<sup>36,37</sup> The only part of the beam transmitted are the wavelengths that interfere constructively within the FPI cavity, which are correlated to the separation between the DBRs as illustrated in Fig. 1. The transmission peaks are much narrower in the case of multiple-beam interferometers which improves the overall measurement accuracy and resolution.<sup>37</sup> In high-performing MEMS-based FPIs, highly reflective quarter-wave thick DBRs are essential for maximizing the optical performance in terms of a high transmission peak, narrow linewidth, and large out-of-band rejection. These DBRs are fabricated using a stack of alternating quarter-wavelength thick layers of high- and low-refractive index materials.<sup>21</sup> The reflectivity of a DBR is a function of the ratio of the indices of the high-index and low-index layers. The number of high- and low-index layer pairs used in a DBR can be denoted by either  $N$ -period for perfectly paired layers or  $N + 1/2$ -periods if there is an additional unpaired layer. The reflectivity of a DBR for  $N$  and  $N + 1/2$ -periods can be calculated as<sup>38,39</sup>

$$R(N) = \left( \frac{1 - n_S \left( \frac{n_H}{n_L} \right)^{2N}}{1 + n_S \left( \frac{n_H}{n_L} \right)^{2N}} \right)^2, \quad (1)$$

and



**Fig. 1** A conceptual representation of an FPI, where the broadband light beam enters a Fabry–Pérot optical cavity of length,  $d$ , and the only part of the beam transmitted are the wavelengths that interfere constructively within the FPI cavity.

Imperfection	Foundation	Imperfection finesse
Spherical curvature		$F_{DS} = \frac{\lambda}{2 \delta d }$
Tilt		$F_{DT} = \frac{\lambda}{\sqrt{3}\delta d}$
Roughness		$F_{DR} = \frac{\lambda}{4.7\delta d}$

**Fig. 2** Imperfections in a Fabry–Pérot filter due to spherical curvature, tilt, and roughness.

$$R\left(N + \frac{1}{2}\right) = \left(\frac{n_S - n_H^2 \left(\frac{n_H}{n_L}\right)^{2N}}{n_S + n_H^2 \left(\frac{n_H}{n_L}\right)^{2N}}\right)^2, \quad (2)$$

where  $n_S$ ,  $n_H$ , and  $n_L$  are the refractive index of the substrate and the high and low index layers, respectively.

The finesse of an ideal FPI, also known as the reflectance finesse of the FPI ( $F_R$ ), is expressed as<sup>29,39,40</sup>

$$F_R = \frac{\pi\sqrt{R}}{1-R}. \quad (3)$$

The performance of MEMS-based FPIs degrades when mirror imperfections such as curvature/distortion, tilt, and thin-film roughness (described in Fig. 2) are present in the DBRs. These imperfections reduce the filter finesse and transmission, which leads to broadening of the FWHM.<sup>29,39–43</sup> The increase in FWHM results in a loss of the effective finesse from  $F_E = F_R$  to a value of  $F_E$  defined as

$$\frac{1}{F_E^2} = \frac{1}{F_R^2} + \frac{1}{F_D^2}, \quad (4)$$

where  $F_D$  is the finesse due to imperfections in an FPI. The effective finesse of an FPI is primarily determined by the reflectance finesse  $F_R$ , provided that  $F_D \gg F_R$ . However, when  $F_D$  is significantly lower than  $F_R$ , the value of  $F_E$  is dominated by  $F_D$ , which results in a drop in the peak transmission, an increase in FWHM, and degradation of the out-of-band rejection of an FPI. The imperfection finesse of the filter can be calculated from

$$\frac{1}{F_D^2} = \frac{1}{F_{DS}^2} + \frac{1}{F_{DT}^2} + \frac{1}{F_{DR}^2} + \dots, \quad (5)$$

where  $F_{DS}$ ,  $F_{DT}$ , and  $F_{DR}$  are the imperfection finesse component due to curvature/distortion, tilt, and thin-film roughness as expressed in Fig. 2.<sup>10,39–42</sup>

When the imperfections of fully-fabricated DBRs are taken into account the linewidth, FSR, and peak transmission of an FPI can be expressed as<sup>39</sup>

$$\delta\lambda = \frac{\lambda}{F_E \left(m + \frac{1}{n_H - n_L}\right)}, \quad (6)$$

$$\Delta\lambda = \frac{\lambda}{\left(m + 1 + \frac{1}{n_H - n_L}\right)}, \quad (7)$$

and

$$T_{FP}(\Psi) \approx \left(\frac{F_E}{F_R}\right) \frac{T_{pk}}{1 + \frac{4F_E^2}{\pi^2} \sin^2\left(\frac{\Psi}{2}\right)}, \quad (8)$$

respectively, where  $T_{pk}$  is the peak transmittance,  $\Psi = 2\pi m$  is the phase at which transmission maxima occur, and  $m$  defines the order of the maxima. The peak transmittance,  $T_{pk}$ , can be expressed as<sup>39,40</sup>

$$T_{pk} = \frac{T^2}{(1 - R)^2}, \quad (9)$$

where  $T = 1 - R - A$ , and  $A$  represents the absorption losses in the DBRs,<sup>39,40</sup> which is assumed to be zero for DBRs based on lossless dielectric thin films.

### 3 FPI Design

A MEMS-based fixed cavity LWIR (8 to 12  $\mu\text{m}$ ) FPI consists of a free-standing top DBR and a bottom DBR on a Si substrate and operates as a bandpass filter with narrow spectral width. Table 1 summarizes the optical layers structure, and design parameters of MEMS-based LWIR FPIs having sizes of 500  $\mu\text{m} \times 500 \mu\text{m}$  and 1 mm  $\times$  1 mm, categorized as  $\alpha$ - and  $\beta$ -series FPIs, respectively. A 3-dimensional exploded view of a surface micromachined fixed cavity FPI is shown in Fig. 3. The four-layer bottom ( $\text{BaF}_2/\text{Ge}/\text{BaF}_2/\text{Ge}$ ) and three-layer top ( $\text{Ge}/\text{BaF}_2/\text{Ge}$ ) DBRs consist of  $\lambda/4$ -thick high (Ge) and low ( $\text{BaF}_2$ ) refractive index thin films of thickness 625 and 1850 nm, respectively, giving a center wavelength of  $\lambda = 10 \mu\text{m}$  as listed in Table 1. A detailed study of the optical and mechanical parameters of Ge and  $\text{BaF}_2$  thin films was presented in our previous work.<sup>34,35</sup> The optical cavity length between the two DBRs was defined by a 5- $\mu\text{m}$ -thick polyimide PI2611 sacrificial layer, which determines the wavelength of the transmission peak. The square top DBR was perforated with an array of etch holes to facilitate the release process as well as diagonally arranged notches in the four corners to minimize the impact of excessive stress arising from lateral orthogonal directions.

Furthermore, to minimize the impact of substrate originating interference fringes within the transmission characteristics a 2-mm-thick Si-substrate was adopted, which provides an interference-free spectral response for the FPI. The backside of the Si-substrate was covered with a 200-nm-thick gold (Au) optical shield to define the optical aperture windows, and subsequently followed by a  $\lambda/4$ -thick  $\text{BaF}_2$  antireflection layer. The Au layer prevents stray light from leaking around the optical aperture onto the detector within the Fourier-transform infrared (FTIR) measurement instrument, and the backside  $\text{BaF}_2$  antireflection coating suppresses the effect of multiple reflections. The square optical aperture windows provide an optical area of 400  $\mu\text{m} \times 400 \mu\text{m}$  and 900  $\mu\text{m} \times 900 \mu\text{m}$  for  $\alpha$ - and  $\beta$ -series FPIs, respectively.

**Table 1** Design parameters and optical layer structure of a MEMS-based fixed cavity LWIR FPI with a center wavelength of 10  $\mu\text{m}$ . Note that the deposited layer thicknesses are within a tolerance of  $\pm 5\%$ .

Entity	LWIR (8 to 12 $\mu\text{m}$ )	
	Material	Thickness (nm)
Top DBR	Ge/ $\text{BaF}_2$ /Ge	625/1850/625
Optical cavity	Air	5 $\mu\text{m}$
Bottom DBR	$\text{BaF}_2$ /Ge/ $\text{BaF}_2$ /Ge	1850/625/1850/625
Substrate	Si	2 mm
Optical shield	Au	200
Antireflection coating	$\text{BaF}_2$	1850

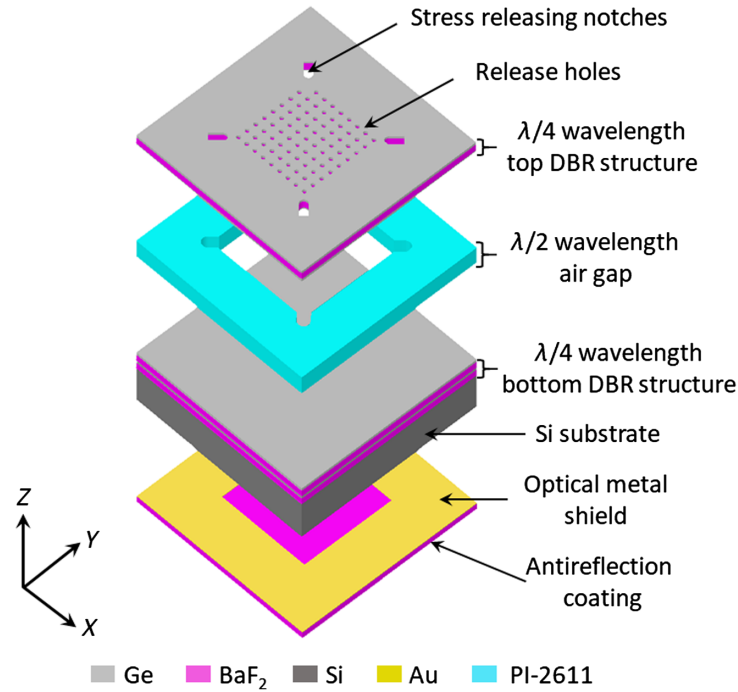


**Fig. 3** Three-dimensional exploded view of the MEMS-based LWIR fixed cavity FPI using Ge/BaF<sub>2</sub> based dielectric DBRs. The antireflection coating and optical shield are also shown. The 5- $\mu\text{m}$ -thick PI-2611 polyimide sacrificial layer is removed only from the optical area and serves as a perimeter support layer to maintain the desired air gap between the top and bottom DBRs.

#### 4 Fabrication of Fixed Cavity Filters

The fabrication process of a fixed cavity FPI commenced with the deposition of a four-layer (BaF<sub>2</sub>/Ge/BaF<sub>2</sub>/Ge) bottom DBR on a 2-mm-thick Si substrate using thermal evaporation as shown in Fig. 4(a). This was followed by an adhesion promoter HD Microsystems VM 651 and HD Microsystems PI-2611 polyimide sacrificial layer [see Fig. 4(b)], which was spin-coated at 3750 rpm. The nominally 5- $\mu\text{m}$ -thick polyimide coating across a 2" Si wafer was measured to be  $4.85 \pm 0.15 \mu\text{m}$  using a Dektak stylus profilometer. This thickness variation in the polyimide layer was  $< \sim 6 \text{ nm}$  within the 1 mm  $\times$  1 mm membrane area. The polyimide was patterned into square islands (4 mm  $\times$  4 mm) using positive photoresist AZ4562 as an etch mask in CF<sub>4</sub>/O<sub>2</sub> plasma. The resulting delineation of FPIs reduces any stress-related effects caused by thermal expansion of the top DBR layers during the membrane release process.<sup>44–47</sup>

In the next step, the three-layer (Ge/BaF<sub>2</sub>/Ge) top DBR was deposited and patterned using a lift-off technique to define the perforation holes that facilitate removal (release) of the polyimide sacrificial layer, and stress releasing notches at each corner of the suspended top DBR [see Fig. 4(c)]. To do so, Sigma-Aldrich hexamethyldisilazane was applied on the polyimide surface followed by positive photoresist AZ4562. The photoresist process was optimized to achieve high aspect ratio features ( $\sim 6\text{-}\mu\text{m}$ -thick and 6- $\mu\text{m}$ -diameter cylinders) to enable the lift-off of unwanted material in the areas that define the etch holes and corner notches. The optimal pattern definition was achieved by spinning AZ4562 photoresist at 3000 rpm and baking it for 11 min at 113°C on a hot plate, followed by UV exposure at a dose of 234 mJ/cm<sup>2</sup> and 80 s development in 1:3 diluted AZ400K with DI water. This was followed by thermal evaporation of Ge/BaF<sub>2</sub>/Ge layers that form the top DBR as shown in Fig. 4(c), and lift-off from the unwanted areas in an acetone bath. Since the total thickness of the top DBR stack was  $> 3 \mu\text{m}$ , the lift-off process consisted of two cycles of 10 min acetone soaking followed by a short ultrasonic treatment after each 10 min soak. It was found that as long as the total thickness of the deposited Ge and BaF<sub>2</sub> layers was  $< 60\%$  of the photoresist thickness, a successful lift-off can be achieved.

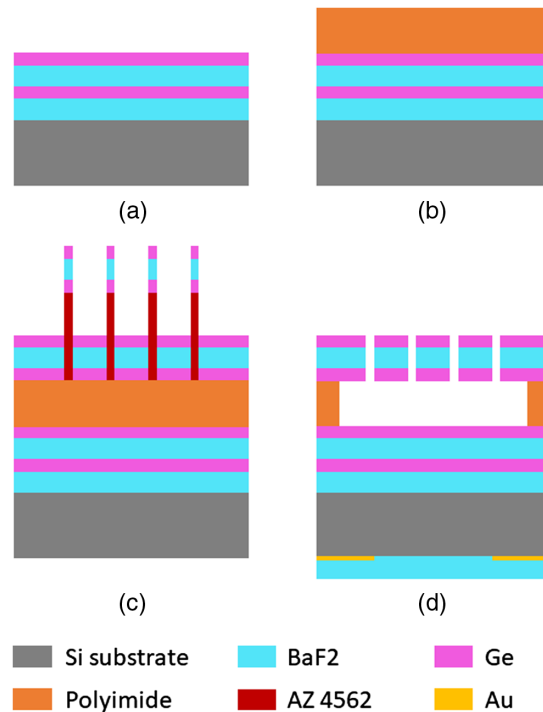


**Fig. 4** Fabrication process flow of fixed cavity FPIs; (a) deposition of a four-layer (BaF<sub>2</sub>/Ge/BaF<sub>2</sub>/Ge) bottom DBR on a 2-mm-thick Si substrate using thermal evaporation; (b) adhesion promoter HD Microsystems VM 651 and HD Microsystems PI-2611 polyimide sacrificial layer; (c) patterning of three-layer (Ge/BaF<sub>2</sub>/Ge) top DBR ( $\sim 3\text{-}\mu\text{m}$  thick) using lift-off and positive photoresist AZ4562 to define release holes for removal of sacrificial layer; and (d) deposition of backside metal shield (Au) and antireflection coating (BaF<sub>2</sub>), and polyimide removal in the oxygen plasma to realize free-standing top DBR.

At this stage, the roughness of the top DBR was measured using atomic force microscopy, giving average and RMS surface roughness values of 48 and 59 nm, respectively.

A 200-nm-thick gold (Au) layer was deposited on the backside of the substrate and patterned using the lift-off technique to define the optical aperture windows, which was followed by a  $\lambda/4$ -thick BaF<sub>2</sub> antireflection coating as shown in Fig. 4(d). It is noted that the front side of the sample was protected with positive photoresist when depositing the backside metal shield and antireflection coating. Finally, to form the air-gap between the top and bottom DBRs, the polyimide sacrificial layer was removed from the optical area in an O<sub>2</sub> plasma [see Fig. 4(d)] in a March PM-600 Barrel Asher with 120 W RF power at 1 Torr chamber pressure. The release process was performed in four consecutive steps of 20 min each to prevent cracks forming in the top DBR due to long-time exposure to the O<sub>2</sub> plasma.<sup>23</sup> Figure 5 shows an optical micrograph of a fully released  $\alpha$ -series FPI. The visible cracks propagating from the sharp corners of the notches are due to long-time exposure to the oxygen plasma, which can be resolved by having all curved notches without any sharp corners.

An FIB scanning electron microscopy (SEM) system was used to verify the release process of the top DBR. Figure 6(a) illustrates the top view of the FPI and the position of the FIB cut is marked with a red line. Figure 6(b) shows the SEM image of the FPI with the exposed top and bottom DBRs, where the cross-section was prepared by the FIB technique. A magnified image of the central area represented by the yellow dashed rectangle in Fig. 6(b) is depicted in Fig. 6(c). The cross-section allowed us to verify if any residues or vestiges of the sacrificial layer were left underneath the top DBR. As expected, the free-standing top membrane/DBR collapsed on the bottom DBR as a result of the FIB cutting process, and hence the cavity gap shown in the picture is not a true representation of the actual air cavity gap. Nevertheless, images do confirm a clean removal of the sacrificial layer in an O<sub>2</sub> plasma.

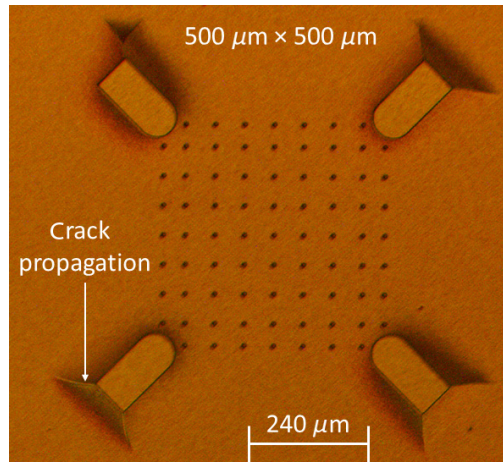


**Fig. 5** An optical microscopic image of a released  $\alpha$ -series FPI. The crack propagation from the sharp corners of notches is due to long-time exposure to the oxygen plasma.

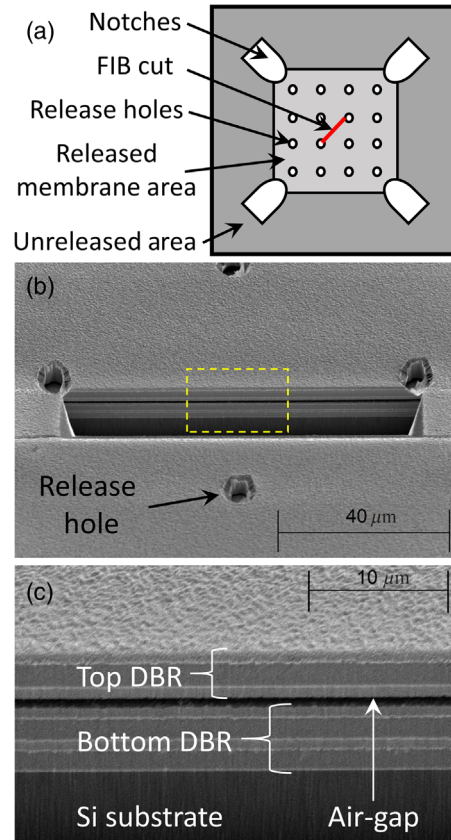


**Fig. 6** Validation of a clean removal of polyimide from the optical area using a FIB-SEM. (a) Representation of the top view of an FPI (not to scale). The red line indicates the position of the FIB cut presented in subfigures (b) and (c). (b) SEM micrograph of FIB cut performed between two diagonally positioned release holes [as depicted in (a)] located near the center of the FPI. (c) A magnified image of the rectangular area is indicated by the yellow dashed rectangle in (b). The cross-section micrograph confirms that there is no residue or vestiges of the sacrificial layer left underneath the top DBR after the release process. Note that the top DBR has collapsed onto the bottom DBR as a result of the FIB process. Therefore, the air gap in (b) and (c) is not a true representation of the Fabry-Pérot cavity length.

## 5 Characterization of Fixed Cavity Filters

Characterization of fully released fixed cavity FPIs was performed using three techniques: optical surface profilometry, laser Doppler vibrometry, and FTIR spectroscopy. Optical surface profilometry was used to determine residual stress of the free-standing thin films and flatness of the top DBR, laser Doppler vibrometry was used to measure the resonant frequency of the released structures, and FTIR was used to characterize the wavelength-dependent optical performance of the FPIs.

### 5.1 Stress in Multilayer Top and Bottom DBRs

Figure 5 shows an optical microscope image of a released  $\alpha$ -series FPI. In order to achieve a very flat suspended top DBR, good control of the in-built thin-film stress is required. Thin-film stress was calculated from Stoney's formula by measuring the change in curvature of a 100- $\mu\text{m}$ -thick Si-substrate pre- and post-deposition of the thin film. In this paper, the cumulative tensile stress for both four-layer bottom and three-layer top DBR thin films stacks was found to be 14 and 23 MPa, respectively. The near-zero stress of the  $\text{BaF}_2$  thin films allowed low tensile stress to be achieved within the multilayer DBR stacks while limiting the sample temperature  $<100^\circ\text{C}$  during Ge deposition. The deposition process and related internal stress of stand-alone Ge and  $\text{BaF}_2$  thin films have been presented in a previous study.<sup>34</sup>

### 5.2 Suspended DBR Flatness Profiles

A white light optical surface profilometer (Zygo Newview 6K) was used to measure the flatness of the suspended DBRs. Figure 7(a) shows the 3D optical surface profile of the fabricated  $\alpha$ -series FPI, where the dashed lines represent the FPI mirror area and solid line AA' represents the corresponding diagonal surface profile line scan as shown in Figs. 7(b)–7(d). Figure 7(b) depicts the measurement profile for both  $\alpha$ - and  $\beta$ -series FPIs. Magnified views of the dotted elliptical area represented in Fig. 7(b) are presented in Figs. 7(c) and 7(d) for  $\alpha$ - and  $\beta$ -series FPIs, respectively. Figures 7(c) and 7(d) confirm that in the optical area of interest, a 10 to 20 nm tilt was observed in the free-standing top DBRs, expressed as  $F_{DT}$  in Eq. (5). It can also be observed that the top DBR exhibits  $\sim 25 \pm 5$  nm of surface roughness after the release process, expressed as  $F_{DR}$  in Eq. (5). An exemplar of observed DBR tilt and surface roughness measurements is shown in Fig. 7(c).

### 5.3 Mechanical Resonance of Suspended Top DBR

The mechanical resonance of the free-standing trilayer top DBR has been characterized using laser Doppler vibrometry (LDV), a noncontact vibration measurement technique based on the difference between two laser beam frequencies: a reference beam from the fixed bottom DBR, and a test beam from the center of the free-standing top DBR. The output response of an LDV is a continuous analog voltage that is directly proportional to the target velocity component in the direction of the laser beam. The samples were placed in a vacuum chamber during measurement and the free-standing top DBRs were excited mechanically using a blue laser to record the resonance frequencies of 218 and 152 kHz for the top DBRs for  $\alpha$ - and  $\beta$ -series FPIs, respectively, as shown in Fig. 8. The mechanical resonance also confirms that the top DBRs of the FPIs were fully released and freely suspended, which cannot occur if there is any remnant polyimide between the top and bottom DBRs.

### 5.4 Transmission Spectra of FPIs

Optical transmission measurements of fixed cavity FPIs were performed using a Perkin Elmer Spotlight 200i FTIR Microscopy System with spectrum two. These experiments were performed with a wavenumber resolution of  $0.5\text{ cm}^{-1}$ , which provided a measurement resolution from 3.2 to 7.2 nm for the wavelength range from 8 to 12  $\mu\text{m}$ , respectively. For the transmission measurements using FTIR, first a reference signal was measured on a reference sample consisting of

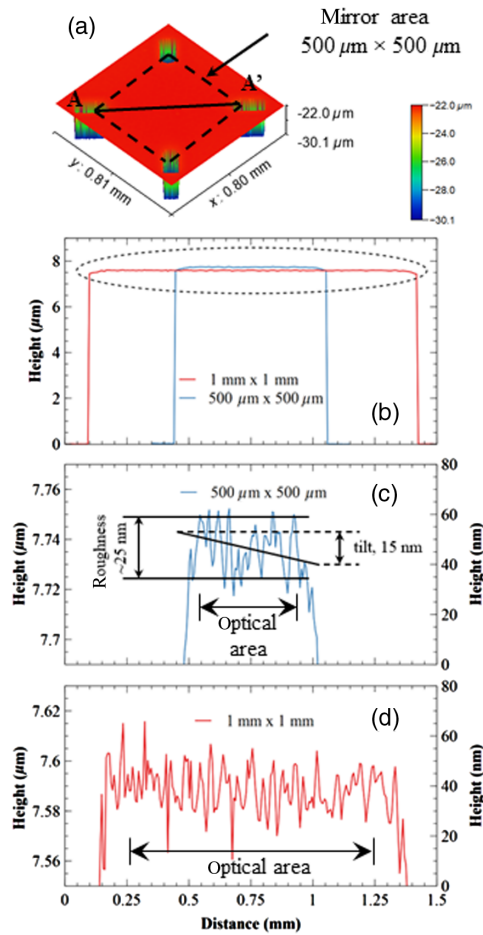


**Fig. 7** Optical surface profiles of  $\alpha$ - and  $\beta$ -series FPIs. (a) 3D surface plot of an  $\alpha$ -series FPI, where the dashed lines represent the mirror area and the diagonal solid line AA' represents the surface profile line scan across the diagonal. (b) The AA' line scan across the diagonal of  $\alpha$ - and  $\beta$ -series FPIs. (c) and (d) Magnified views of the dotted region represented in (b) for  $\alpha$ - and  $\beta$ -series FPIs, respectively.

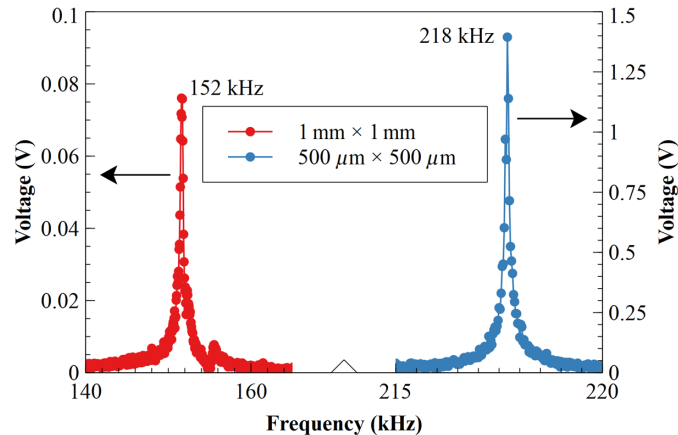


**Fig. 8** Mechanical resonance of free-standing three-layer top DBRs using LDV for  $\alpha$ -series (blue plot) and  $\beta$ -series (red plot) DBRs.

**Table 2** Comparison between measured and modeled optical performance (including nonideal effects; tilt – 15 nm and surface roughness – 25 nm) of  $\alpha$ - and  $\beta$ -series FPIs.

No. of devices	Device parameters	Center wavelength ( $\mu\text{m}$ )	Peak $T_x$ (%)		FWHM (nm)	
			Modeled	Measured	Modeled	Measured
Five separate devices	$\alpha$ -series (500 $\mu\text{m} \times 500 \mu\text{m}$ )	$9.33 \pm 0.03$	48	$40.5 \pm 1.5$	97	$116.5 \pm 5.5$
Five separate devices	$\beta$ -series (1 mm $\times$ 1 mm)	$9.2 \pm 0.1$	48	$47 \pm 2.5$	97	$109.5 \pm 2.5$

an optical shield and antireflection coating on one side of a silicon substrate of the same type used for the fabricated FPIs. For measurements on FPI devices, a beam of collimated light is directed onto the optical area of the filters and the transmitted signal as a function of wavelength is measured by a detector placed on the other side of the sample. As noted previously, 2-mm-thick Si-substrates were adopted in this study to minimize the impact of substrate originating interference fringes within the measured optical performance of an FPI that would be present if standard 300- $\mu\text{m}$ -thick Si-substrates had been used during high-resolution FTIR measurements.<sup>48–50</sup>

The spectral transmission measurements were performed on 10 devices comprising five separate samples from each of the  $\alpha$ - and  $\beta$ -series FPIs, with the results summarized in Table 2. Figure 9 depicts the measured spectral transmission of  $\beta$ -series FPIs measured using the FTIR, and compares it with the modeling results calculated using the matrix method modeling technique.<sup>51</sup> The solid lines represent the modeled FPI spectral transmission including top mirror imperfections such as tilt and surface roughness, as noted previously (see Fig. 7), whereas the data points depict the measured transmission. The transmission response is plotted linearly in percentage and logarithmically in dB units, as depicted in Figs. 9(a) and 9(b), respectively, to present the out-of-band rejection performance. It is noted that the information provided in

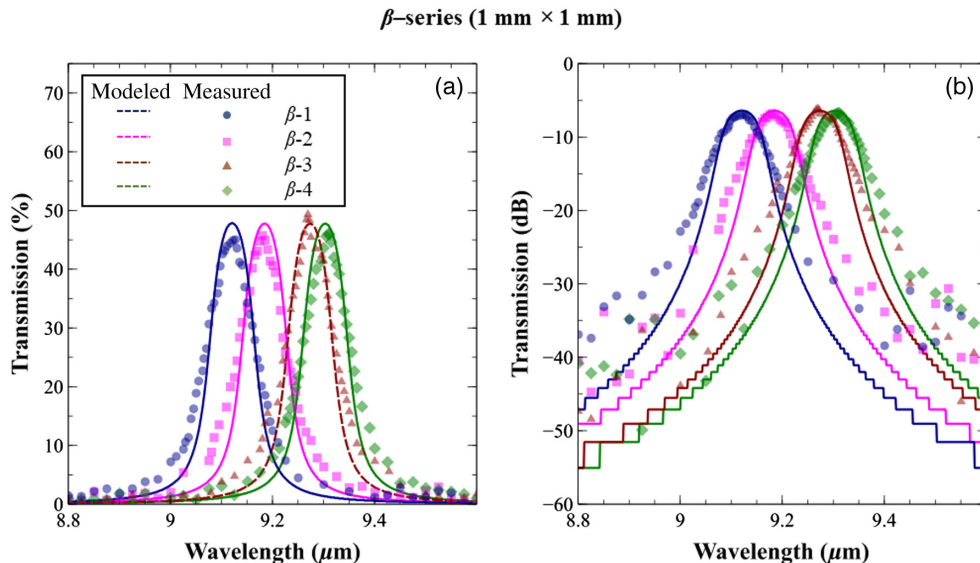


**Fig. 9** A comparison of measured and modeled spectral transmission of  $\beta$ -series FPIs. The solid lines represent the modeled performance including nonideal effects (tilt – 15 nm and surface roughness – 25 nm) using the matrix method, and the data points represent the measured FPIs spectral transmission. The transmission response was plotted (a) linearly in percentage and (b) logarithmically in dB units to present the out-of-band rejection performance. It is noted that the information provided in the legend of (a) is also valid for (b). The variation in sacrificial layer thickness between individual devices leads to the observed variation in peak transmission wavelength from 9.1 to 9.3  $\mu\text{m}$ .

the legend of Fig. 9(a) is also valid for Fig. 9(b). In order to represent the transmission peak clearly, Fig. 9 includes the optical characteristics of four different  $\beta$ -series FPIs, and it is noted that very similar results were obtained for the  $\alpha$ -series FPIs. The measured transmission spectral response for  $\beta$ -series fixed cavity FPIs gave a peak transmission approaching 50% with a peak wavelength of  $9.2 \pm 0.1 \mu\text{m}$ , and FWHM of  $\sim 110 \text{ nm}$ , as shown in Table 2 and Fig. 9(a). The measured data presented in Fig. 9(b) shows that an out-of-band rejection ratio of  $\geq 30 \text{ dB}$  can be achieved for  $\beta$ -series FPIs in comparison to simulated out-of-band rejection ratio of  $>40 \text{ dB}$ . A good agreement is noted between the measured and modeled response of FPIs, and that similar results were obtained on  $\alpha$ -series FPIs.

It is important to note that curvature/distortion and/or tilt are only of relevance to the fully suspended top DBRs. Since the bottom DBRs were directly deposited on the thick Si-substrate, it can be assumed that no curvature/distortion and/or tilt is present in the bottom DBRs. Although 20 nm of curvature/distortion or tilt alone does not significantly affect the optical response of the fabricated FPIs, it is the combination of several factors that starts to play a crucial role in degrading the optical performance. Surface roughness in thin films significantly degrades the optical performance of an FPI, leading to broadening of the transmission band and a drop in the peak transmission. Based on the measurements performed of witness samples after deposition, it was observed that the total roughness of the top DBR is mainly dominated by the roughness of the thermally deposited  $\text{BaF}_2$  film, which can be significant when few micrometer-thick layers are deposited. This roughness can be reduced by utilizing alternative physical vapor deposition techniques such as pulsed laser deposition, sputtering, and E-beam deposition. Furthermore, the optical performance of these FPIs is likely to be affected by nonfiltered light passing through release holes to the detector and by diffraction effects. Although this topic is beyond the scope of the current study, it is well known that the nonfiltered light passing to the detector can be blocked by adding light-blocking metal pads under the release holes.<sup>12,21</sup> Also, these light-blocking metal pads further help to reduce the diffraction effects.

Table 3 shows a comparison of the peak transmission and FWHM of surface micro-machined FPIs reported in this work with previously reported FPIs in the LWIR spectral band. It is important to note that this work presents fixed cavity FPIs that do not incorporate a MEMS-based actuation mechanism for the top DBR, thus a comparison of the tuning range is not relevant. However, this work can be compared with previously reported work for peak transmittance and FWHM. It is clear from Table 3 that the use of silicon and air as high- and low-refractive index materials/media, respectively, has allowed Tuohiniemi et al.<sup>18,19</sup> to achieve an FWHM of 140 nm and a peak transmission in the range of 40% to 60%.

Similarly, Mao et al.<sup>21–23</sup> used Ge and ZnS as the high- and low-refractive index layers, which allowed them to achieve an FWHM of 500 to 1000 nm and a peak transmission of 38% to 87%. These devices had been developed for LWIR multispectral imaging rather than spectroscopic sensing applications, with a targeted FWHM of 5% to 10% of the passband peak wavelength. Since the refractive index values for Ge and ZnS are 4 and 2.2, respectively, the relatively low refractive index contrast limits the possibility of achieving narrower FWHM. Therefore, in the current work, the ZnS low-refractive index layer has been replaced with  $\text{BaF}_2$  having a refractive index of 1.35 in the LWIR region, which provides the high index contrast required for narrowband FPIs. In addition, the Ge single-layer top mirror used by Mao et al.<sup>21–23</sup> has been replaced with a three-layer top DBR ( $\text{Ge}/\text{BaF}_2/\text{Ge}$ ), which has allowed the achievement of a narrowband FPI having an FWHM of 110 nm and a peak transmission of  $\sim 50\%$ .

**Table 3** Comparison of results from this work with earlier reported studies on surface micro-machined air-cavity MEMS-based LWIR FPIs.

Wavelength region	DBR materials	Wavelength range ( $\mu\text{m}$ )	Peak $T_x$ (%)	FWHM (nm)	References
LWIR	Si/Air/Si	Tunable 7.6–11.24	40 to 60	140	18 and 19
	Ge/ZnS/Ge	Tunable 8.5–11.5	38 to 87	500 to 1000	21–23
	Ge/ $\text{BaF}_2$ /Ge	Fixed $9.2 \pm 0.1$	$\sim 50$	110	This work

**Table 4** A comparison between the required, long-term targeted, and achieved spectral characteristics for FPIs for LWIR spectroscopic sensing applications.

Parameter	Required	Long-term target	Achieved	
			$\alpha$ -series (500 $\mu\text{m} \times 500 \mu\text{m}$ )	$\beta$ -series (1 mm $\times$ 1 mm)
Peak transmission	$\gtrsim 50\%$	$\gtrsim 80\%$	$\gtrsim 40\%$	$\sim 50\%$
FWHM	$\lesssim 150$ nm	$\lesssim 100$ nm	115 nm	110 nm
Out-of-band rejection	$\gtrsim 50:1$	$\gtrsim 50:1$	$\gtrsim 30:1$	$\gtrsim 30:1$

Table 4 provides a comparison of the measured spectral transmission characteristics with the long-term target values, as well as with the optical requirements of FPIs for LWIR spectroscopic sensing applications. The MEMS-based fixed cavity FPIs presented in this paper provide a platform technology for future development of narrowband and high throughput tunable FPIs, which can be further improved by minimizing the roughness of the thin film DBR layers.

## 6 Summary and Conclusions

We have demonstrated prototype fixed cavity FPIs in the LWIR spectral band, based on Ge/BaF<sub>2</sub> thin-film DBRs. The measured spectral response for 500  $\mu\text{m} \times 500 \mu\text{m}$  devices showed a peak transmission of  $\sim 40\%$  and an FWHM of  $\sim 115$  nm for a center wavelength value  $\sim 9.34 \mu\text{m}$ . Similarly, for 1 mm  $\times$  1 mm fixed cavity FPIs, the peak transmission was  $\sim 50\%$  with an FWHM of  $\sim 110$  nm for a center wavelength value  $\sim 9.27 \mu\text{m}$ . After the inclusion of measured values for tilt and surface roughness of 15 and 25 nm, respectively, the measured optical characteristics of the FPIs were in good agreement with the modeled optical response. The drop in peak transmission and broadening of spectral passband was observed mainly to be due to the high surface roughness of the BaF<sub>2</sub> layer, which can be improved by depositing higher quality, uniform, and smooth layers of BaF<sub>2</sub>.

## Acknowledgments

This work used the facilities of the Western Australian node of the NCRIS-enabled Australian National Fabrication Facility (ANFF), a company established under the National Collaborative Research Infrastructure Strategy to provide nano- and microfabrication facilities for Australia’s researchers and support from the Western Australian Government’s Department of Jobs, Tourism, Science and Innovation. This research work was supported financially by the Australian Research Council (ARC), including ARC Centre of Excellence on Transformative Meta-Optical Systems (TMOS). The authors also thankfully acknowledge the Centre for Microscopy, Characterisation & Analysis (CMCA); and The University of Western Australia for offering Scholarship for International Research Fees; and The Microelectronics Research Group (MRG) for an Ad Hoc Postgraduate Scholarship. There is no conflict of interest.

## References

1. R. V Chimenti, *The New Technologies Shaping Near-Infrared Spectroscopy*, Laurin Publishing (2020).
2. A. Näsilä et al., “Cubic-inch MOEMS spectral imager,” *Proc. SPIE* **10931**, 109310F (2019).
3. A. Rissanen et al., “Hand-held MEMS hyperspectral imager for VNIR mobile applications,” *Proc. SPIE* **10545**, 105450R (2018).
4. H. Saari et al., “Novel miniaturized hyperspectral sensor for UAV and space applications,” *Proc. SPIE* **7474**, 74741M (2009).

5. *Selection Guide: Mini-Spectrometers*, pp. 1–7, Hamamatsu Photonics K.K., [https://www.hamamatsu.com/content/dam/hamamatsu-photonics/sites/documents/99\\_SALES\\_LIBRARY/ssd/mini-spectro\\_kacc0002e.pdf](https://www.hamamatsu.com/content/dam/hamamatsu-photonics/sites/documents/99_SALES_LIBRARY/ssd/mini-spectro_kacc0002e.pdf) (2020).
6. J. R. Silva et al., “Large area silicon-air-silicon DBRs for infrared filter applications,” *J. Lightwave Technol.* **37**(3), 769–779 (2019).
7. A. J. Das et al., “Ultra-portable, wireless smartphone spectrometer for rapid, non-destructive testing of fruit ripeness,” *Sci. Rep.* **6**, 32504 (2016).
8. M. Martyniuk et al., “Optical microelectromechanical systems technologies for spectrally adaptive sensing and imaging,” *Adv. Funct. Mater.* **32**, 2103153 (2021).
9. H. A. Macleod, *Thin-Film Optical Filters*, 2nd ed., Adam Hilger Ltd, Bristol (1986).
10. P. D. Atherton et al., “Tunable Fabry–Pérot filters,” *Opt. Eng.* **20**(6), 806–814 (1981).
11. J. S. Milne et al., “Widely tunable MEMS-based Fabry–Pérot filter,” *J. Microelectromech. Syst.* **18**(4), 905–913 (2009).
12. D. K. Tripathi et al., “Large-area MEMS-based distributed bragg reflectors for short-wave and mid-wave infrared hyperspectral imaging applications,” *J. Microelectromech. Syst.* **24**(6), 2136–2144 (2015).
13. D. K. Tripathi et al., “Modelling and Characterization of the MEMS based filters for the spectroscopic imaging applications,” in *Conf. Optoelectron. and Microelectron. Mater. and Devices, COMMAD 2018*, pp. 43–46 (2018).
14. B. Saadany et al., “Electrostatically-tuned optical filter based on silicon Bragg reflectors,” in *IEEE/LEOS Int. Conf. Opt. MEMS and Their Appl. Conf.*, pp. 86–87 (2006).
15. H. Saari et al., “Visible, very near IR and short wave IR hyperspectral drone imaging system for agriculture and natural water applications,” *ISPRS - Int. Arch. Photogramm. Remote Sens. Spat. Inf. Sci.* **XLII-3/W3**, 165–170 (2017).
16. T. Kääriäinen et al., “Active hyperspectral sensor based on MEMS Fabry–Pérot interferometer,” *Sensors* **19**(9), 2192 (2019).
17. A. Akujärvi et al., “MOEMS FPI sensors for NIR-MIR microspectrometer applications,” *Proc. SPIE* **9760**, 97600M (2016).
18. M. Tuohiniemi, A. Näsälä, and J. Mäkynen, “Characterization of the tuning performance of a micro-machined Fabry–Pérot interferometer for thermal infrared,” *J. Micromech. Microeng.* **23**, 075011 (2013).
19. M. Tuohiniemi et al., “Optical transmission performance of a surface-micromachined Fabry–Pérot interferometer for thermal infrared,” *J. Micromech. Microeng.* **22**(11), 115004 (2012).
20. H. Mao et al., “Towards longwave infrared tuneable filters for multispectral thermal imaging applications,” 2014, [www.ndt.net/?id=17694](http://www.ndt.net/?id=17694) (accessed 15 April 2020).
21. H. Mao et al., “Large-Area MEMS Tunable Fabry–Pérot Filters for Multi/Hyperspectral Infrared Imaging,” *IEEE J. Sel. Top. Quantum Electron.* **23**(2), 2700208 (2017).
22. H. Mao et al., “MEMS-based tunable Fabry–Pérot filters for adaptive multispectral thermal imaging,” *J. Microelectromech. Syst.* **25**(1), 227–235 (2016).
23. H. Mao et al., “Ge/ZnS-based micromachined Fabry–Pérot filters for optical MEMS in the longwave infrared,” *J. Microelectromech. Syst.* **24**(6), 2109–2116 (2015).
24. M. Ebermann et al., “Widely tunable Fabry–Pérot filter based MWIR and LWIR microspectrometers,” *Proc. SPIE* **8374**, 83740X (2012).
25. N. Neumann et al., “Uncooled IR sensors with tunable mems Fabry–Pérot filters for the long-wave infrared range,” in *Proc. IEEE Sens.*, pp. 2383–2387 (2010).
26. M. Ebermann et al., “Tiny mid- and long-wave infrared spectrometer module with a mems dual-band Fabry–Pérot filter,” in *IRS2 Proc. - Sens.+Test Conf.*, pp. 94–99 (2011).
27. M. Meinig et al., “Tunable mid-infrared filter based on Fabry–Pérot interferometer with two movable reflectors,” *Proc. SPIE* **7930**, 79300K (2011).
28. M. Meinig et al., “Dual-band MEMS Fabry–Pérot filter with two movable reflectors for mid- and long-wave infrared microspectrometers,” in *16th Int. Solid-State Sens., Actuators and Microsyst. Conf., TRANSDUCERS’11*, pp. 2538–2541 (2011).
29. M. Ebermann et al. “Recent advances in expanding the spectral range of MEMS Fabry–Pérot filters,” *Proc. SPIE* **7594**, 75940V (2010).
30. W. Gunning et al., “MEMS-based tunable filters for compact IR spectral imaging,” *Proc. SPIE* **7298**, 72982I (2009).

31. P. A. Stupar et al., “MEMS tunable Fabry–Pérot filters with thick, two sided optical coatings,” in *TRANSDUCERS 2009-2009 Int. Solid-State Sens., Actuators and Microsyst. Conf.*, pp. 1357–1360 (2009).
32. W. Kaiser et al., “Infrared properties of CaF<sub>2</sub>, SrF<sub>2</sub>, and BaF<sub>2</sub>,” *Phys. Rev.* **127**(6), 1950–1954 (1962).
33. M. R. Query, *Optical Constants of Minerals and Other Materials from the Millimeter to the Ultraviolet*, Aberdeen Proving Ground, Maryland (1987).
34. G. S. Gill et al., “Ge/BaF<sub>2</sub> thin-films for surface micromachined mid-wave and long-wave infrared reflectors,” *J. Opt. Microsyst.* **2**(1), 011002 (2022).
35. G. S. Gill et al., “Mechanical properties of thermally evaporated germanium (Ge) and barium fluoride (BaF<sub>2</sub>) thin-films,” *MRS Commun.* **12**, 112–118 (2022).
36. J. Vaughan, *The Fabry–Pérot Interferometer: History, Theory, Practice, and Applications*, A. Hilger, Bristol, UK; Philadelphia (1989).
37. H. A. Macleod, *Thin-Film Optical Filters*, 4th ed., pp. 1–782 (2010).
38. E. Garmire, “Theory of quarter-wave-stack dielectric mirrors used in a thin Fabry–Pérot filter,” *Appl. Opt.* **42**(27), 5442 (2003).
39. J. S. Milne, *Micro-Electromechanical Technologies For Next-Generation Spectroscopic Systems*, The University of Western Australia, Perth, Western Australia (2009).
40. L. P. Schuler et al., “MEMS-based microspectrometer technologies for NIR and MIR wavelengths,” *J. Phys. D Appl. Phys.* **42**, 133001 (2009).
41. R. M. Hill, “Some Fringe-broadening defects in a Fabry–Pérot Étalon,” *Opt. Acta Int. J. Opt.* **10**(2), 141–152 (1963).
42. J.-S. Moon and A. M. Shkel, “Performance limits of a micromachined tunable-cavity filter,” in *Proc. Int. Conf. MSM*, pp. 278–281 (2001).
43. G. J. Sloggett, “Fringe broadening in Fabry–Pérot interferometers,” *Appl. Opt.* **23**(14), 2427 (1984).
44. W. Fang and C. Y. Lo, “On the thermal expansion coefficients of thin films,” *Sens. Actuators, A Phys.* **84**(3), 310–314 (2000).
45. T. Walewyns et al., “Polyimide as a versatile enabling material for microsystems fabrication: surface micromachining and electrodeposited nanowires integration,” *J. Micromech. Microeng.* **23**, 095021 (2013).
46. K. L. Brookshire et al., “Investigation of thermal expansion effects on Si-based MEMS structures,” *J. Microelectromech. Syst.* **25**(3), 549–556 (2016).
47. G. Abadias et al., “Review article: Stress in thin films and coatings: current status, challenges, and prospects,” *J. Vac. Sci. Technol. A* **36**, 20801 (2018).
48. B. Harbecke, “Coherent and Incoherent reflection and transmission of multilayer structures,” *Appl. Phys. B* **39**, 165–170 (1986).
49. S. W. King and M. Milosevic, “A method to extract absorption coefficient of thin films from transmission spectra of the films on thick substrates,” *J. Appl. Phys.* **111**, 73109 (2012).
50. S. Maung, P. Kaung, and S. Htoon, “The Fourier transform and FTIR system as a technique in semiconductor research,” *J. Myan. Acad. Arts Sci.* **II**(2) (2004).
51. J. Silva et al., “Method for optical modelling of non-uniform and non-parallel multi-thin film MEMS optical filters and mirrors,” in *Conf. Optoelectron. and Microelectron. Mater. and Devices, COMMAD 2018*, pp. 35–38 (2018).

**Gurpreet Singh Gill** received his BTech and MTech degrees in electronics and communication engineering from Punjab Technical University and Sri Guru Granth Sahib World University, Punjab, India, in 2013 and 2015, respectively. He is currently pursuing a PhD in the Department of Electrical, Electronic and Computer Engineering, The University of Western Australia, Perth, Western Australia, Australia. His current research activities involve thin-film materials and optical micro-electro-mechanical systems for multi-/hyper-spectral imaging and sensing applications.

**Michał Zawierła** received his BSc and MSc degrees in electronics and telecommunication from the Wrocław University of Technology, Wrocław, Poland, in 2011 and 2012, respectively, and his PhD in electrical and electronics engineering from The University of Western Australia,

Perth, Western Australia, Australia. He is currently a research fellow with the Microelectronics Research Group at The University of Western Australia, Perth, Western Australia, Australia. His current research activities involve optical microelectromechanical systems.

**Dhirendra Kumar Tripathi** received his BTech degree in electronics engineering from Uttar Pradesh Technical University, Lucknow, India, in 2005, his MTech degree in VLSI systems from National Institute of Technology, Tiruchirappalli, India, in 2008, and his PhD from The University of Western Australia, Perth, Western Australia, Australia, in 2016. He is currently a postdoctoral researcher at The University of Western Australia. His research activities involve design and fabrication of optical MEMS devices and materials for the MEMS.

**Adrian Keating** received his BE and PhD degrees in electrical and electronic engineering from the University of Melbourne, Australia, in 1990 and 1995, respectively. In 2004, he joined the School of Electrical, Electronic and Computer Engineering, University of Western Australia, Perth, Australia, moving to the School of Mechanical Engineering in 2007. He is currently an associate professor with research activities in the field of optical microelectro-mechanical systems, porous silicon-based sensor technologies, and the internet-of-things.

**Gino Putrino** received his BSc degree in computer science and his BE degree in electrical and electronic engineering from The University of Western Australia, Perth, Western Australia, Australia, in 1999 and his PhD degree in 2014. His research interests involve the use of optical microelectro-mechanical systems (MEMS) and silicon photonics to create novel chemical and biological sensing devices.

**K. K. M. B. Dilusha Silva** received the honours degrees in physics and electronic engineering from The University of Western Australia (UWA), Perth, Western Australia, Australia, and his PhD in optical imaging technologies for biomedical applications in 2004. He has worked both in industry and academia, and is currently with the Microelectronics Research Group, UWA. His research interests included optical MEMS sensors, optical spectroscopic sensors, and atmospheric optics.

**Lorenzo Faraone** received his PhD from The University of Western Australia (UWA), Perth, Western Australia, Australia, in 1979. He joined the School of Electrical, Electronic and Computer Engineering, UWA, in 1987, where he has been a professor since 1998, and the head of the Department/School from 1999 to 2003. Since joining UWA, his research interests have been in the areas of compound semiconductor materials and devices, and microelectromechanical systems.

**Mariusz Martyniuk** received his BSc (Hons.) degree from the University of Toronto, his MASc from McMaster University, and his PhD from The University of Western Australia in 2007. He worked in the industry sector as an electronics engineer before re-joining The University of Western Australia, where he is currently with the Microelectronics Research Group and manages the Western Australian Node of the Australian National Fabrication Facility. His primary areas of interest encompass thin-film materials and thin-film mechanics, as well as their applications in micro-electromechanical systems and optoelectronic devices.